Integrated photonic power divider with arbitrary power ratios

KE XU,[1,*] LU LIU,[1] XIANG WEN,[1] WENZHAO SUN,[1] NAN ZHANG,[1] NINGBO YI,[1] SHANG SUN,[1] SHUMIN XIAO,[1,2] AND QINGHAI SONG[1]

[1]Harbin Institute of Technology (Shenzhen), HIT Campus, The University Town of Shenzhen, Xili, Shenzhen 518055, China
[2]e-mail: shuminxiao@hitsz.edu.cn
*Corresponding author: kxu@hitsz.edu.cn

Integrated optical power splitters are one of the fundamental building blocks in photonic integrated circuits. Conventional multimode interferometer-based power splitters are widely used as they have reasonable footprints and are easy to fabricate. However, it is challenging to realize arbitrary split ratios, especially for multi-outputs. In this Letter, an ultra-compact power splitter with a QR code-like nanostructure is designed by a nonlinear fast search method. The highly functional structure is composed of a number of freely designed square pixels with the size of 120×120 nm which could be either dielectric or air. The light waves are scattered by a number of etched squares with optimized locations, and the scattered waves superimpose at the outputs with the desired power ratio. We demonstrate 1×2 splitters with 1:1, 1:2, and 1:3 split ratios, and a 1×3 splitter with the ratio of 1:2:1. The footprint for all the devices is only 3.6×3.6 μm. Well-controlled split ratios are measured for all the cases. The measured transmission efficiencies of all the splitters are close to 80% over 30 nm wavelength range.   © 2017 Optical Society of America

OCIS codes: (130.0130) Integrated optics; (130.3120) Integrated optics devices; (130.3990) Micro-optical devices.

https://doi.org/10.1364/OL.42.000855

Photonic integrated circuits (PICs) have become a new paradigm for an on-chip subsystem with a plethora of applications such as optical computing [1,2], interconnection [3–6], and sensing [7,8]. Similar to the electronic integrated circuits, the success of the PIC originates from the large-scale integration of various devices and functionalities on a single chip. As one of the most fundamental building blocks in a PIC, the power splitters/combiners are widely used in many optical circuits. In the past, the multimode interferometer (MMI) has been a preferred candidate for this function due to its compactness, large optical bandwidth, and excellent fabrication tolerance. Normally, a passive MMI divides the power equally to each output according to the principle of self-imaging.

However, an arbitrary split ratio attracts more interest for many purposes such as signal monitoring, feedback circuits, and power equalization. To realize this function using the MMI, the device structure needs either sophisticated modifications to break the symmetry or tuning schemes. Specially designed asymmetric MMI has been demonstrated with a split ratio other than unity for 1×2 splitter [9,10], but it is difficult to design a multi-output splitter due to the increased design complexity. Adding an electro-optic tuning element also allows the realization of arbitrary split ratios and could be applied to a multi-output device [11]. The cost will be increased in this case as the electro-optic tuning elements require more fabrication steps, and the power consumption will be significantly larger. Directional coupler is an alternative while cascaded a multi-stage coupler is needed for multiple outputs, and the operation bandwidth is quite limited by the phase matching condition. Though much effort has been made, the existing design philosophy relies too much on the physical laws and the design experience. Actually, the design space is hardly fully explored in this case.

There are quite a few optimization methods developed to search the parameter space, rather than sweeping and fine tuning a very limited number of parameters. Objective-first topology optimization [12] has recently been applied to design the wavelength multiplexer [13] and mode multiplexers [14]. A genetic algorithm was used to design a resonator [15] and grating coupler [16]. A compact 3 dB coupler based on particle swarm optimization has also been reported [17]. A similar algorithm that relied on discretized pixel direct searching has been reported to design the polarization beam splitter [18], bending [19], and coupler [20] with very compact sizes. Recently, we also demonstrated a barcode-like waveguide fiber coupler using a fast search method (FSM) which is capable of dealing with multi-objectives [21]. Thus far, all the above design strategies are based on dielectric permittivity engineering in a deep subwavelength scale and, hence, generate an optimum structure according to the specification. Since the electronic design automation in integrated circuits has achieved a huge success, it is believed that such automation would be promising and revolutionary for advanced photonic circuits.

In this Letter, we have demonstrated a compact power divider/combiner using a QR code-like structure which, to the best of our knowledge, could achieve arbitrary power split ratio for the first time. To the best of our knowledge, this is the first all-passive multi-output power splitter that could potentially achieve arbitrary split ratios. The device structure is optimized by the FSM using a normal desktop. Compared with the topology optimization method, the advantage of this method is that the minimum device feature (pixel) size could be defined according to the nano-patterning resolution.

Silicon photonics is one of the most promising platforms for PIC due to many remarkable advantages. Thus, we design the device on the silicon on insulator (SOI) substrate with 220 nm of top silicon and 3 μm of buried oxide (BOX). The splitter is divided into 30 × 30 pixels, and each of them is a square of 1 20 nm × 120 nm which could be easily fabricated using state-of-the-art lithography and a dry etching technique. To this end, all the devices we are discussing below have the same size of 3.6 μm × 3.6 μm. The pixels have a binary state of the dielectric property: silicon or air. We start from an all-silicon structure which is a normal MMI to initialize the optimization process depicted as Fig. 1(a). We switch one pixel state in each iteration to determine whether the pixel state should be silicon or air. Hence, the refractive index could be engineered at every location of the device in a deep subwavelength scale. Then a few figure-of-merits (FOMs) are defined and numerically calculated by 3D finite difference time domain simulation. They are the transmission efficiency at the i-th output (E_i) and the power ratios between the ith and $(i + 1)$th output (α_i). Specially, the TE mode light is launched into the input single-mode waveguide, and the monitors are used to measure the power at the output waveguides. The algorithm keeps searching the structure until the FOMs reach to a certain value. The values of FOMs are our objectives which have been defined prior to the simulation. Apart from maximizing the power at all the output ports, the power ratios should also be strictly controlled by different convergence conditions. Thus, it becomes a multi-objective problem. If all the FOMs are improved, the state of the pixel is saved. Otherwise, the state

is reversed, and the program proceeds to the next pixel. The convergence conditions in our algorithm are described by

$$\left(\frac{\sum_i E_{i,j+1}}{\sum_i E_{i,j}} > 1\right) \text{AND} \left[\left(\frac{E_{i+1,j+1}}{E_{i,j+1}} - \alpha_i\right)^2 < \rho_{i,j+1}^2\right], \quad (1)$$

where $E_{i,j}$ stands for the transmission efficiency of the i-th output waveguide in the j-th iteration and $\rho_{i,j+1}$ is the radius of convergence for the ith split ratio and $(j + 1)$th iteration. Here we apply an FSM to speed up the parameter searching which could be referred to in [21]. Since a fast rate of convergence usually requires a strong convexity of the objective [22], an elliptical equation (a function of E and α) is used to approximate the radius of convergence ρ_j when the transmission efficiency is below a certain threshold. Afterward, a linear function is used to approximate the ρ_j when the efficiency is higher. Finally, the device is optimized for a wide range of wavelengths to ensure a broad band operation. The optimized structure has a number of unintuitively located square holes, and the schematic picture of a 1 × 3 splitter is shown by Fig. 1(b).

We use a normal four-core desktop to design the device by automatically running the program. The computation cost is ~120 h in average to get the optimized structure. The simulated electric fields at a wavelength of 1550 nm are plotted in Fig. 2. The power dividing mechanism for this type of structure is different from the conventional MMI splitter. The launched electromagnetic waves reach the unintuitively located scattering center, and the scattered waves superimpose at the output waveguides. The desired power split ratio could be achieved by a proper structure. We first design three 1 × 2 power splitters with three different ratios of 1:1 (device 1), 1:1.5 (device 2), and 1:2 (device 3) to show the possibility of precise split ratio control. The simulated electric fields for the optimized structures are shown in Figs. 2(a)–2(c). Compared with the 1 × 2 splitter, the realization of a multi-output power splitter with arbitrary power ratios would be more attractive. The design method in this Letter could be applied to a more general case with arbitrary split ratios and an arbitrary number of output ports in principle. Here we show a proof-of-concept demonstration of a 1 × 3 splitter with a splitting ratio of 1:2:1 (device 4). The electric field distribution for the optimum structure is simulated and shown in Fig. 2(d). A higher intensity could be observed at the central output waveguide than at the other two ports. The simulated power split ratios over a wide wavelength range are shown in Figs. 3(a) and 3(b) for the 1 × 2 and 1 × 3 splitters, respectively. A negligible error of the split ratio over the wavelength range from 1530 to 1560 nm is observed. The algorithm we developed has a good control on the split ratios with acceptable errors for the 1 × 2 splitters over a 30 nm wavelength range. Here we have not considered the operation bandwidth as an objective. It could be improved further for
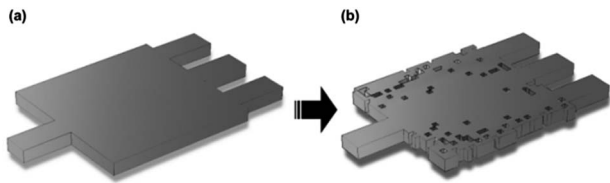
Fig. 1.   (a) Schematic picture of the normal all-silicon MMI structure for initialization. (b) Schematic picture of the optimized structure.
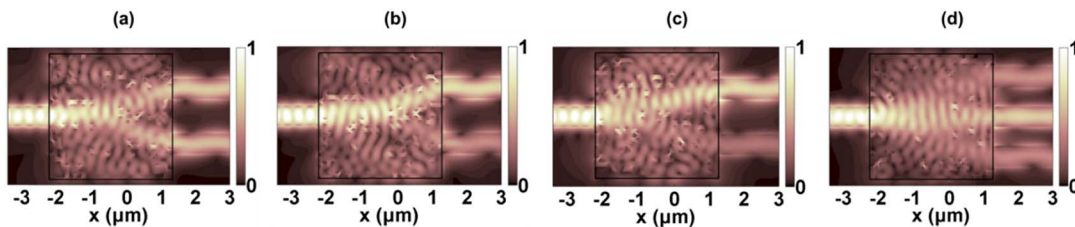
Fig. 2.   (a)–(d) Simulated electric fields for optimized devices 1–4, respectively.
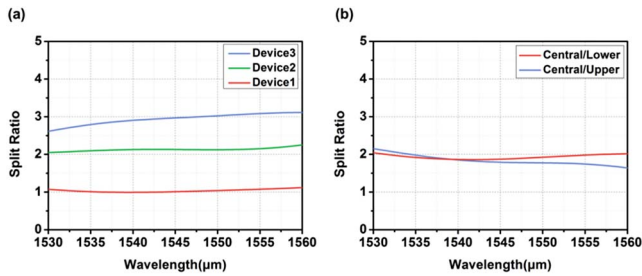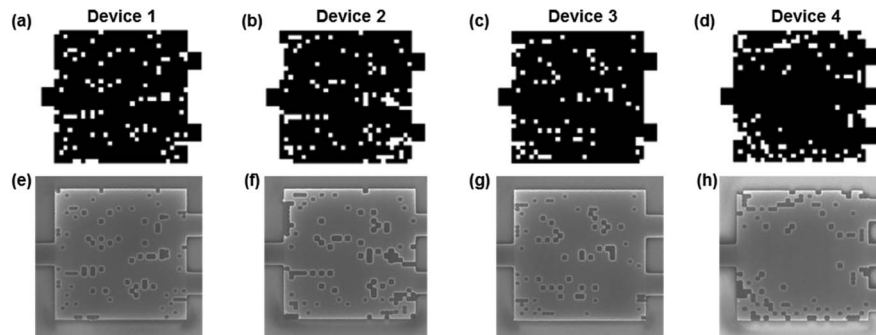
Fig. 3. (a) Simulated split ratios for the 1 × 2 splitters (devices 1–3). (b) Simulated power split ratio for the 1 × 3 splitter (device 4), where the blue line indicates the simulated power ratio between the central port and the upper port. The red line indicates the ratio between the central port and the lower port.

wide band operation, while the computation cost will be higher at the same time by setting another objective. The splitting ratio of the 1 × 3 splitter is plotted in Fig. 3(b) where the red line indicates the ratio between the central output port and the lower output port. The blue line describes the ratio between the central port and the upper output port. Both ratios equal 2:1, as we expect, but there is a small discrepancy at a longer wavelength. This could be improved if we increase the optimization time. It should be noted that the simulated transmission efficiencies of all the devices are ~80% within the whole

spectrum range from 1530 to 1560 nm. The excess loss is expected to mainly come from the scattering of each etched holes.

The above devices are fabricated on a commercial SOI wafer (SOITEC, Inc.) with 220 nm of top silicon and 3 μm of BOX. The device layout is patterned by electron beam lithography (Raith eLINE) which operates at 30 kV. The positive photoresist ZEP 520A is used as the mask. The pattern is then transferred in the device layer using a one-step inductively coupled plasma etch process. The power splitter has a small footprint of only 3.6 μm × 3.6 μm. The schematic search optimized structures are shown in Figs. 4(a)–4(d) which correspond to devices 1–4. The white square indicates the etched air holes located within the device area. The top-view scanning electron microscope (SEM) images of the fabricated devices are shown in Figs. 4(e)–4(h). Though some of the squares have round corners due to the imperfection of the fabrication process, the following experimental results actually indicate good robustness of the designs. The experiment is carried out to evaluate the device functionality and performance. Continuous wave light from a tunable laser is coupled into the submicron waveguide through a subwavelength focusing grating coupler with a 10° tilt. The coupling loss is measured to be ~7 dB per grating at the peak wavelength. It is a bit higher than the simulated loss, and this is due to the fabrication errors induced by the etching process. It could be improved further by a non-uniform period or shallow etched structure. The output power at each port is then


Fig. 4. (a)–(d) QR code-like device geometry for devices 1–4 with the power split ratios of 1:1, 1:2, 1:3, and 1:2:1, respectively. (e)–(h) SEM images of the devices 1–4, correspondingly.
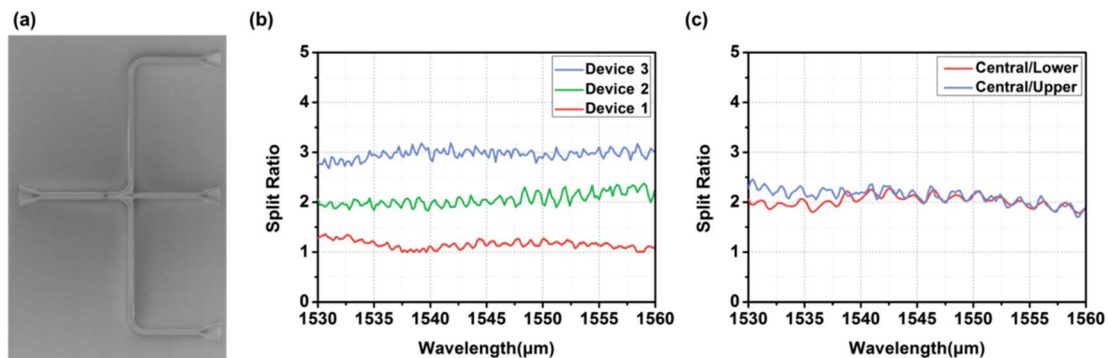
Fig. 5. (a) Top-view SEM of the whole device. (b) Measured split ratio for the 1 × 2 splitter (devices 1–3). (c) Measured power split ratio for the 1 × 3 splitter (device 4). The blue line indicates the measured power ratio between the central port and the upper port. The red line indicates the ratio between the central port and the lower port.
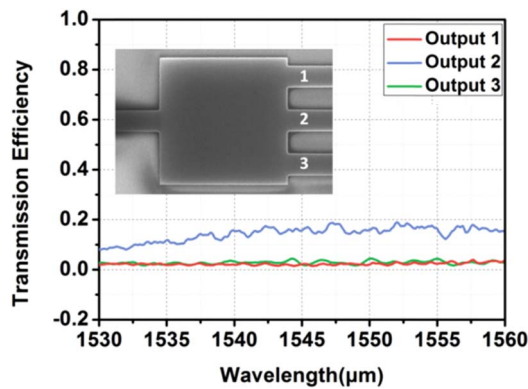
Fig. 6. Measured transmission efficiencies of output ports 1–3 of the all-silicon conventional MMI. Inset: the top-view SEM image of the device.

measured by a photodetector after coupling out the light from the chip with another grating coupler. The top-view SEM of a whole 1 × 3 splitter is shown in Fig. 5(a). The 1 × 2 power splitter is characterized by scanning the wavelength and recording the output power ratio between each port. The measured results of devices 1–3 are plotted in Fig. 5(b). Flat responses for the three devices are obtained over a 30 nm spectrum range. The measured results are consistent with the objectives we set. Devices 1 and 3 have a larger error at a short wavelength near 1530 nm, but this agrees with the predictions from simulations. The power split ratio of the 1 × 3 splitter (device 4) is measured and is shown in Fig. 5(c). It depicts the power ratio between the central output and the upper/lower output which both should be 2:1. The measured transmission efficiencies of devices 1–4 are quite close to 80% from 1530 to 1560 nm. By optimizing the etching recipe, we believe these values could reach the theoretical values. Thus far, we have successfully demonstrated a series of power splitters with the target split ratios.

On the other hand, the optimum transmission efficiency of a conventional MMI splitter is highly dependent on the splitter geometry, especially the length of the multimode region. However, our method has realized both 1 × 2 and 1 × 3 splitters with different split ratios and the same size which are hardly possible for normal MMI. This is a significant promise to broaden the current device library developed by the formal design method and to establish a new device design fashion. To validate the contributions from the unintuitively located squares, we have done a control experiment by fabricating a conventional all-silicon MMI. The all-silicon MMI has the same geometry as device 4 (3.6×3.6 μm^2) and has three output ports. The top-view SEM image of the all-silicon normal MMI is shown in the inset of Fig. 6. We also measured the transmission efficiencies of each port and the split ratio. The measured transmission efficiencies of output ports 1–3 are plotted in Fig. 6. It turns out that the efficiencies are quite low without the pixels that are etched. The central output port has nearly 20% efficiency, while the other two ports have less than 5% efficiency. In addition, the split ratio is far from what

we designed. In this sense, our optimization algorithm works well, and the QR code-like nanostructure is found to be highly efficient and functional.

To conclude, we have experimentally demonstrated a potential technique to achieve an integrated optical power splitter with an arbitrary ratio. The device is optimized by a fast searching method with a reasonable computing cost. To the best of our knowledge, this is the first demonstration of a passive silicon power splitter with multi-output ports which are optimized by an algorithm. We have shown three 1 × 2 splitters with a ratio of 1:1, 1:2, and 1:3. To demonstrate the scalability for multi-output operation, we also report a 1 × 3 splitter with a ratio of 1:2:1. The experimental results are consistent with the simulation results and have negligible errors from the design targets. This Letter demonstrates the possibility of the design automation for realization of a highly functional device that is hardly possible for a conventional first-principle design philosophy.

REFERENCES

1. F. Liu, T. Wang, L. Qiang, T. Ye, Z. Zhang, M. Qiu, and Y. Su, Opt. Express **16**, 15800 (2008).
2. F. Xia, L. Sekaric, and Y. Vlasov, Nat. Photonics **1**, 65 (2007).
3. K. Xu, Z. Cheng, C. Y. Wong, and H. K. Tsang, Opt. Lett. **37**, 4738 (2012).
4. P. Dong, X. Liu, S. Chandrasekhar, L. Buhl, R. Aroca, and Y.-K. Chen, IEEE J. Sel. Top. Quantum Electron. **20**, 6100108 (2014).
5. K. Xu, L. G. Yang, J. Y. Sung, Y. M. Chen, Z. Cheng, C. W. Chow, C. H. Yeh, and H. K. Tsang, J. Lightwave Technol. **31**, 2550 (2013).
6. N. Sherwood-Droz, H. Wang, L. Chen, B. G. Lee, A. Biberman, K. Bergman, and M. Lipson, Opt. Express **16**, 15915 (2008).
7. M. Lee and P. M. Fauchet, Opt. Express **15**, 4530 (2007).
8. A. Densmore, D.-X. Xu, S. Janz, P. Waldron, T. Mischki, G. Lopinski, A. Delage, J. Lapointe, P. Cheben, B. Lamontagne, and J. H. Schmid, Opt. Express **33**, 596 (2008).
9. Q. Deng, L. Liu, X. Li, and Z. P. Zhou, Opt. Lett. **39**, 5590 (2014).
10. A. Zanzi, A. Brimont, A. Griol, P. Sanchis, and J. Marti, Opt. Lett. **41**, 227 (2016).
11. J. Leuthold and C. H. Joyner, J. Lightwave Technol. **19**, 700 (2001).
12. J. Lu and J. Vuckovic, Opt. Express **20**, 7221 (2012).
13. A. Y. Piggot, J. Lu, K. G. Lagoudakis, J. Petykiewicz, T. M. Babinec, and J. Vuckovic, Nat. Photonics **9**, 347 (2015).
14. L. F. Frellsen, Y. Ding, O. Sigmund, and L. H. Frandsen, Opt. Express **24**, 16866 (2016).
15. A. Gondarenko and M. Lipson, Opt. Express **16**, 17689 (2008).
16. J. Covey and R. T. Chen, Opt. Express **21**, 10886 (2013).
17. J. C. C. Mak, C. Sideris, J. Jeong, A. Hajimiri, and J. K. S. Poon, Opt. Lett. **41**, 3868 (2016).
18. B. Shen, P. Wang, R. Polson, and R. Menon, Nat. Photonics **9**, 378 (2015).
19. B. Shen, R. Polson, and R. Menon, Opt. Lett. **40**, 5750 (2015).
20. B. Shen, P. Wang, R. Polson, and R. Menon, Opt. Express **22**, 27175 (2014).
21. X. Wen, K. Xu, and Q. Song, Photon. Res. **4**, 209 (2016).
22. D. Garber and E. Hazan, in *Proceedings of International Conference on Machine Learning* (2015), Vol. **37**.